

Quantifying the electrochemical kinetics of battery positive-electrode crystal facets

Received: 1 April 2025

Accepted: 1 October 2025

Published online: 20 November 2025

Xu Li¹, Jun Huang², Le Yang¹, Hao-Sen Chen¹ , Wei-Li Song¹ ,
Shuqiang Jiao^{1,3,4} & Daining Fang¹

Improving the reaction kinetics of $\text{LiNi}_{0.8}\text{Mn}_{0.1}\text{Co}_{0.1}\text{O}_2$ is of great importance for realizing batteries with both high energy and power density. The promotion of electrochemical kinetics, i.e. exchange current density of $\text{LiNi}_{0.8}\text{Mn}_{0.1}\text{Co}_{0.1}\text{O}_2$ materials, is a significant strategy. Because there is great variation in exchange current density of different crystal facets, it is critical to fundamentally understand the intrinsic exchange current density of crystal facets for designing high-rate electrode materials. To quantitatively analyze the intrinsic exchange current density of six representative crystal facets on $\text{LiNi}_{0.8}\text{Mn}_{0.1}\text{Co}_{0.1}\text{O}_2$ particles, we develop a quantitative single-particle method based on the combination of the electrochemical impedance spectrum and three-dimensional geometric reconstruction on the single-particle scale. Here we show, compared to the exchange current density of (003) facet of $\text{LiNi}_{0.8}\text{Mn}_{0.1}\text{Co}_{0.1}\text{O}_2$ particles, interestingly, the exchange current density of (201) facet exhibits a 25-fold higher value (-1.50 mA/cm^2), which is used to guide the nano-structure design of anisotropic core-shell $\text{LiNi}_{0.8}\text{Mn}_{0.1}\text{Co}_{0.1}\text{O}_2$ particles with improved rate performance (500 cycles) at discharge rate of 10 C (6 min).

In the increasing market of electric vehicles, it is urgently required to substantially promote the power and energy density of lithium-ion batteries (LIBs) for achieving fast charging and long mileage^{1,2}. Some positive electrode materials, particularly $\text{LiNi}_{0.8}\text{Mn}_{0.1}\text{Co}_{0.1}\text{O}_2$ (NMC811), are considered as the emerging materials for high energy density. For realizing both high energy and power density capabilities of LIBs, it is critical to improve the kinetics of ion intercalation reaction of both positive electrodes and negative electrodes if the electrode thickness is remained³. As a result, increasing the intrinsic electrochemical kinetics of NMC811 materials is one of strategies to release higher capacity at high rate^{4,5}, in term of reducing the polarization of porous electrodes⁶.

To achieve the goals, in NMC811 particles, promotion of the electrochemical kinetics, i.e., exchange current density (j_0), is one of the significant approaches because j_0 substantially influences the deintercalation/intercalation rate of Li-ion across the particle-

electrolyte interface⁷. For example, the porous electrode using NMC111 particles with an exchange current density -1.5 mA/cm^2 presents a discharge capacity $-104 \text{ mAh}\cdot\text{g}^{-1}$ at 5 C, while the one with an exchange current density -0.6 mA/cm^2 delivers a discharge capacity $-85 \text{ mAh}\cdot\text{g}^{-1}$ at 5 C (at the similar electrode thickness)⁶. To rationally increase the j_0 of NMC811 particles, it is essential to fundamentally analyze each $j_{0(\text{Facet})}$ (defined as the j_0 of the facets on the particle scale in this work) of representative facets on the NMC811 surface, because j_0 of NMC811 particles is understood as the statistical analysis of all the representative $j_{0(\text{Facet})}$ on the particle surface (Fig. 1). Compared with the electrochemical method upon macroscopic porous electrodes (known as the electrode scale for statistical analysis of aggregated NMC811 particles), measurement of the electrochemical kinetics on a single particle scale is considered the powerful base to analyze the $j_{0(\text{Facet})}$ in a more accurate way⁸. Several electrochemical methods have been developed for quantitatively studying the charge transfer kinetics

¹Institute of Advanced Structure Technology, Beijing Institute of Technology, Beijing, P. R. China. ²Institute of Energy and Climate Research, IEK-13: Theory and Computation of Energy Materials, Forschungszentrum Jülich GmbH, Jülich, Germany. ³State Key Laboratory of Advanced Metallurgy, University of Science and Technology Beijing, Beijing, P. R. China. ⁴State Key Laboratory of Advanced Processing and Recycling of Non-ferrous Metal, Lanzhou University of Technology, Lanzhou, P. R. China. e-mail: chenhs@bit.edu.cn; weilis@bit.edu.cn; sjiao@ustb.edu.cn

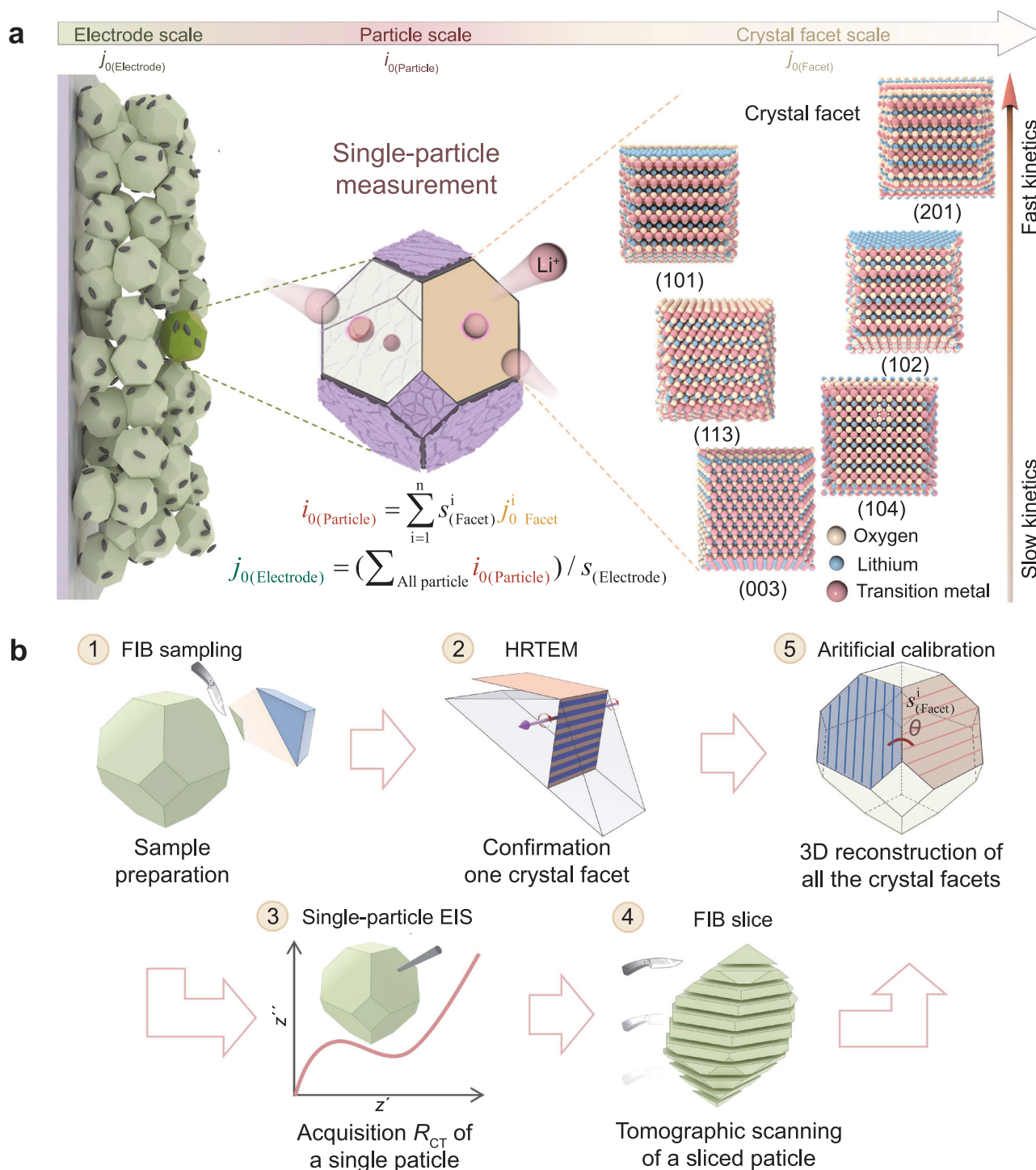


Fig. 1 | Relation of exchange current density at different scales and the method for quantitatively identifying the $j_{0(\text{Facet})}$ of crystal facets. a Three types of j_0 (or i_0) at three different scales, i.e., $j_{0(\text{Electrode})}$, $i_{0(\text{Particle})}$ and $j_{0(\text{Facet})}$.

b Experimental identification of $j_{0(\text{Facet})}$ for quantitative kinetics of six representative crystal facets using single-particle measurements.

at the single-particle scale. For example, scanning electrochemical cell microscopy (SECCM) is used for determining the exchange current density of single LiFePO_4 particles at different discharge states⁹, and it could be also used to map the activity of crystal facets via reducing the diameter of the micropipettes¹⁰. In addition, fluorescence spectroscopy is helpful to investigate the activity of active particles, and TiO_2 nanorods could be scanned to study both electron- and hole-driven photoelectrocatalytic activities under illumination¹¹. Although the characterization of electrochemical kinetics of a single particle has

been well established to date^{12,13}, there is still a great challenge to identify the quantitatively $j_{0(\text{Facet})}$ for crystal facets, because it is difficult to recognize the facet types of each particle.

To overcome such bottlenecks, here we report a quantitative single-particle electrochemical method (Fig. 1). In a typical operation, the electrochemical impedance spectra (EIS) of six single-crystalline particles were experimentally analyzed, followed by three-dimensional (3D) geometric reconstruction of each particle to measure the surface area for six representative crystal facets. Following the calibration of

crystal facets, the corresponding intrinsic $j_{0(\text{Facet})}$ of each crystal facet on the NMC811 particle surface is identified. The quantitative results suggest that the (201) facet of NMC811 exhibits the fastest kinetics for Li^+ intercalation, and the rate of 1.50 mA/cm^2 is 25-fold higher than that of the (003) facet (rate -0.06 mA/cm^2). By understanding such a principle, we have proposed a NMC811 particle with an anisotropic core-shell nanostructure to get rid of the reaction between the slowest (003) facet and electrolyte. The as-assembled LIBs deliver high-rate performance (144 mAh g^{-1} over 500 cycles at a discharge rate of 10 C), which is enhanced compared to the isotropic NMC811 materials.

Results and discussion

Quantitative identification of $j_{0(\text{Facet})}$ for each crystal facet

Porous electrodes composed of active particles are widely applied in commercial LIBs¹⁴. The active particles act as the basic reactive units and their electrochemical properties determine the performance of the LIBs¹⁵. To clarify the exchange current density (j_0) on the different scales, three types of j_0 (or i_0) have been defined and their relations are provided in Fig. 1a. On the porous electrode scale, the exchange current density ($j_{0(\text{Electrode})}$) is the sum of the exchange current of all the active particles ($i_{0(\text{Particle})}$ on the particle scale) per unit projection area of porous electrode (Fig. 1a). The corresponding relation between the electrode scale and particle scale could be described as

$$j_{0(\text{Electrode})} = \left(\sum_{\text{All particles}} i_{0(\text{Particle})} \right) / S_{(\text{Electrode})} \quad (1)$$

where $S_{(\text{Electrode})}$ is the projection area of porous electrode. The interfacial reaction rate of active particles is associated with the exposed crystal facets^{16–19}. On the particle scale, $i_{0(\text{Particle})}$ represents the total current density of all the exposed crystal facets $j_{0(\text{Facet})}$ of a single particle.

$$i_{0(\text{Particle})} = \sum_{i=1}^n S_{(\text{Facet})}^i j_{0(\text{Facet})}^i \quad (2)$$

where $S_{(\text{Facet})}$ is the geometric area of a specific crystal facet on the particle surface, the superscript i represents the different crystal facets. Therefore, characterization of $j_{0(\text{Facet})}$, i.e., the absolute value of current density of cathodic reaction or anodic reaction at the unit area of crystal facet in the equilibrium state, of different crystal facets is significant in the reasonable design of crystal facets. These values are critical to guide in enhancing the rate performance of LIBs.

To measure the intrinsic electrochemical kinetic parameters of $j_{0(\text{Facet})}$, advanced nanotechnologies were combined as shown in Fig. 1b. Specifically, powder X-ray diffraction (XRD) was initially performed for analyzing the main crystals of NMC811 particles (Fig. 2a). Subsequently, high-resolution transmission electron microscope (HRTEM) was carried out for determining the typical crystal facet of one slice cut from a single particle (Figs. 1b, 2c–2d). Furthermore, single-particle electrochemical impedance spectroscopy (EIS) was used for calibrating the $i_{0(\text{Particle})}$ (Fig. 2b) of each NMC811 particle. Furthermore, three-dimensional reconstruction of the corresponding particles was performed via tomographic scanning of the sliced particles (Supplementary Fig. 1). Thereby, the surface areas of each crystal facet on the single particle could be calculated (Figs. 1 and 2e). Using the as-established single-particle measurements on six particles, $j_{0(\text{Facet})}$ of six representative crystal facets with distinct atomic arrangements of NMC811 particles were acquired (Figs. 1a and 2f).

The corresponding experimental results of the six particles are presented in Figs. 2a–2e and Supplementary Fig. 1. The single-particle EIS curves were fitted using an equivalent circuit model (ECM). In such a model, R_s represents the resistance in the loops, R_{CT} and CPE_{CT} refer to the interfacial charge transfer process, and W refers to the Warburg

diffusion process (Fig. 2b). The parameters of each component in ECM and measured $i_{0(\text{Particle})}$ are listed in Supplementary Table 2. According to the results, there is great difference in various $i_{0(\text{Particle})}$, because the exposed crystal facets on each particle surface are diverse.

The crystal facets with consistent atomic arrangement are marked with the same color in Fig. 2e. To determine the area of each exposed facet (either rough or smooth) from the three-dimensional reconstruction images, two methods were used, i.e., measurement of projection areas of the facets and measurement of the surface areas of the facets (the area in a three-dimensional space). These two methods are schemed in Supplementary Fig. 2, and the corresponding measured areas for each particle facet are listed in Supplementary Table 3. The j_0 of the crystal facets was calculated using these two area values, and the obtained results were then converted into the error bars in Fig. 2f. Figure 2f displays the experimental measured $j_{0(\text{Facet})}$ of the representative crystal facets. The $j_{0(003)}$ is 0.06 mA/cm^2 , much smaller than $j_{0(\text{Facet})}$ of the other crystal facets. Among these six types of crystal facets, the largest value is obtained from $j_{0(201)}$ (1.50 mA/cm^2), i.e., a 25-fold higher value than $j_{0(003)}$. Since the goal is to develop a method for measuring the $j_{0(\text{Facet})}$ of NMC811 positive electrode (rather than all of $j_{0(\text{Facet})}$ of NMC811 positive electrode), a certain number of NMC811 particles are selected. Because the selection of particles is random, the results of the selected NMC811 particles are sufficient to exhibit the $j_{0(\text{Facet})}$ of the six representative crystal facets. Note that the other low-index crystal facets of NMC811 positive electrode without identifying in the characterization, such as (110) facet, may be ignored in the identification. As is known, the NMC811 particle exhibits a hierarchical structure with an alternating cycle of transition metal and Li atom layer. The angles between the (003) facet and other crystal facets, i.e., regarded as the angle between transition metal layers on each facet, were displayed in Fig. 2f. Note that the larger angle with the transition metal layer leads to larger $j_{0(\text{Facet})}$ of the crystal facet. For Li-ion transport in the NMC lattices, the energy barrier of transport perpendicular to the (003) is higher than that parallel to (003), which indicates that the probability for Li-ion diffusion perpendicular to the (003) is smaller, or known as weak reactivity. In the experiment on the particle scale, EIS techniques for measuring a quasi-equilibrium state allow for monitoring the small current signal on the (003) facet, i.e., 0.06 mA/cm^2 according to our measurement. Such a value is much smaller than those obtained on the other facets ($> 0.28 \text{ mA/cm}^2$). More importantly, these intrinsic exchange current densities in NMC811 facets are also experimentally identified in this work. According to the value comparison, such a tiny value of $j_{0(003)}$ may be ignored in the experiments using other technologies beyond particle scale.

To evaluate the reliability of such single-particle measurements for determining $j_{0(\text{Facet})}$, three additional particles were tested (detailed data for these three particles is provided in Supplementary Figs. 3–5). Subsequently, the measured and calculated values for charge transfer resistance (R_{CT}) were evaluated, as plotted in Fig. 2g. The calculated values (R_{CT}) were based on $j_{0(\text{Facet})}$ from different crystal facets, and the measured values (R_{CT}) were extracted from the EIS spectra by fitting the equivalent circuit. In these three particles, the difference between the calculated R_{CT} and measured R_{CT} is within 20%. In the previous literature, the difference of $j_{0(\text{Electrode})}$ for LIBs is generally greater than one order of magnitude in value. Therefore, the values of $j_{0(\text{Facet})}$ obtained from the single-particle measurement here are experimentally acceptable.

Mechanism of dominated factors in determining $j_{0(\text{Facet})}$ on the facets

To clarify the origins of distinct kinetic behaviors on the different facets, the ion intercalation kinetic is described using an adiabatic electron-coupled ion transfer model²⁰. In this model, the process of ion transfer from the electrolyte phase to the solid phase has been focused. It also involves transport and desolvation of the lithium ions

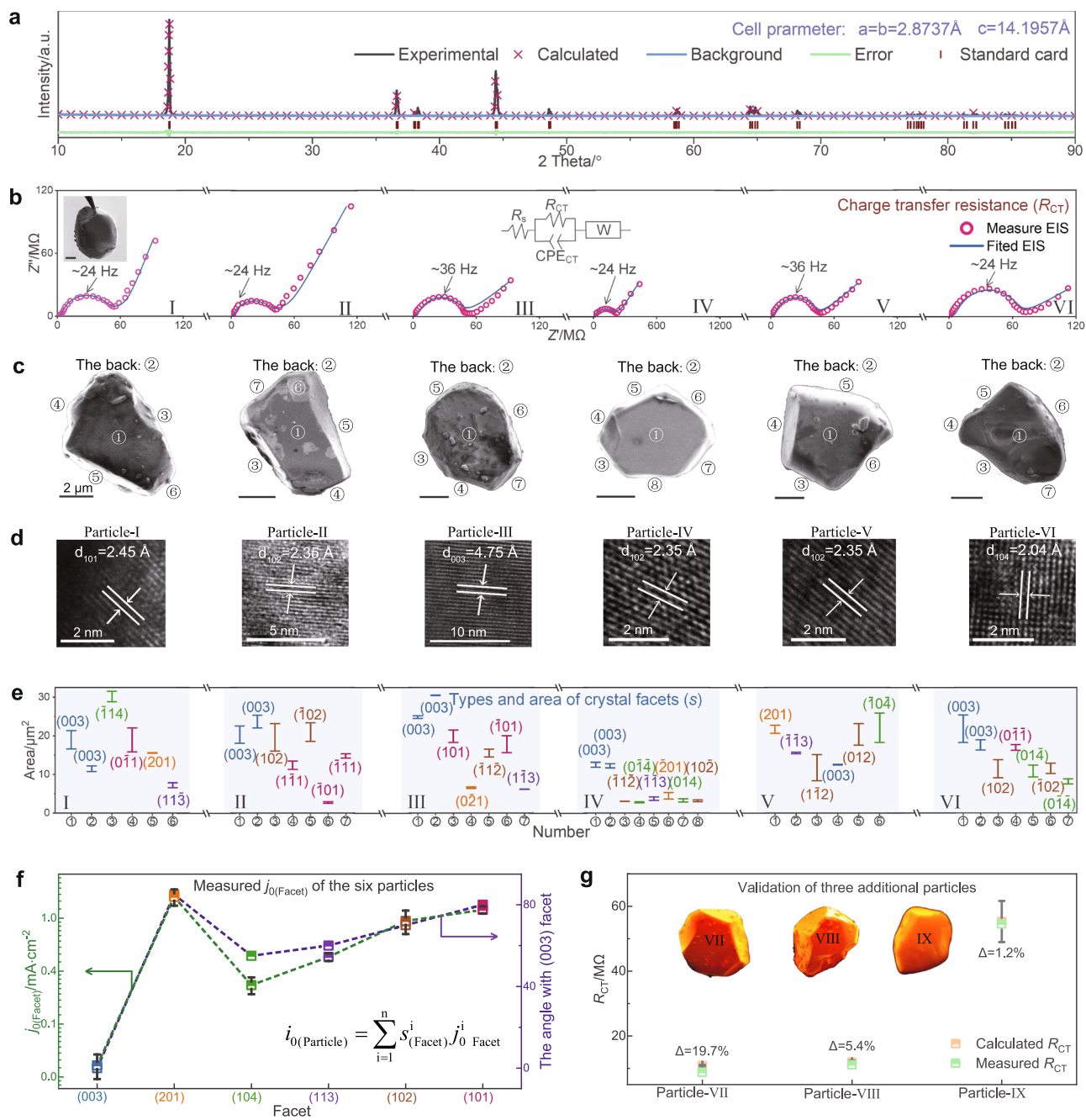


Fig. 2 | Experimental measurement of $j_{0(\text{Facet})}$ of different crystal facets in single NMC811 particles. a The XRD of NMC811 positive-electrode material. **b** The single-particle EIS of six particles (the values for all elements in the equivalent circuit and the numerical errors are provided in Supplementary Table 2). **c** The SEM of six particles (scale bar: 2 μm). **d** The HRTEM of six particles. **e** The types and area of

crystal facets of six particles (the error bars origin from two methods of calculating area). **f** The $j_{0(\text{Facet})}$ measured by single-particle measurements and the angle between these crystal facets and (003) facet. **g** Comparison of the measured and calculated R_{CT} of additional three particles.

in a heterogeneous electric double layer, and electronic interactions between the solid surface and the lithium ions. The latter factor, i.e., electronic interactions, assists in the desolvation process via partially occupying the valence orbital and thus reducing the charge of the lithium ion. The ion transport in the bulk phase of the host material is not considered in this model^{21,22}. In this model, the ion transport in the bulk phase of the host material is not considered, and the single-electron description is used while the electron correlation effects are ignored in the Model Hamiltonian^{21,22}. The description of electrode-electrolyte interface is based on the continuum model and the effects of cathode electrolyte interphase (CEI) are not considered. Recently, Bazant et al.^{22,23} developed a nonadiabatic coupled ion-electron

transfer theory. The key difference between the Bazant's theory and the present model lies in the consideration of electronic interactions, which are revealed to be an important factor in understanding the different kinetics at different facets.

In the adiabatic electron-coupled ion transfer model, potential of zero charge (PZC) affects the potential of crystal facets (ϕ_{Facet}), and thus the distribution of electric field near the crystal facets. The electronic interaction between Li^+ and crystal facet (defined as Δ_0) affects the charge of lithium ions. These two factors (PZC and Δ_0) are the essential parameters to calculate E_a using the above model (Supplementary Fig. 6). Currently, there is not a general theoretical expression for PZC and it cannot be accurately calculated or measured.

Fortunately, PZC is proportional to the work function (WF), and therefore, the WF of each crystal facet was put into the electrical double layer (EDL) model to calculate ϕ_{Facet} according to Eq. (3):

$$\phi_{\text{Facet}} = E_{\text{Positive-electrode}} - \text{WF}/e_0 \quad (3)$$

where $E_{\text{Positive-electrode}}$ (vs. vacuum) acts as a reference potential which is taken according to the potential of the NMC811 positive electrode. Supplementary Fig. 7 presents the Δ_0 , WFs calculated by DFT (the atomic coordinates are provided in Supplementary Data 1), w_{Li^+} , and λ calculated by the EDL model of the six crystal facets. Note that a typical cross-sectional view of the EDL model was simulated by Comsol Multiphysics 5.6, as shown in Supplementary Fig. 8. Also, the data for fitting the Δ_0 of six crystal facets are given in Supplementary Figs. 9–14. According to the transition state theory, $j_{0(\text{Facet})}$ is correlated with E_a as

$$\ln \left(\frac{j_{0(\text{Facet})}}{j_{0(\text{Facet})}^{\text{ref}}} \right) \propto -\frac{E_a - E_a^{\text{ref}}}{k_B \cdot T} \quad (4)$$

where $j_{0(\text{Facet})}^{\text{ref}}$ and E_a^{ref} are the exchange current density and activation barrier of a reference facet-(003) facet, respectively. Adopting the form of Eq. (4) avoids the uncertainty associated with the pre-exponential factor in the Arrhenius equation. Figure 3b presents the ratios of $j_{0(003)}/j_{0(003)}$, $j_{0(201)}/j_{0(003)}$, $j_{0(104)}/j_{0(003)}$, $j_{0(113)}/j_{0(003)}$, $j_{0(102)}/j_{0(003)}$, and $j_{0(101)}/j_{0(003)}$, in which $j_{0(003)}$ is considered as the $j_{0(\text{Facet})}^{\text{ref}}$.

The trend of measured $\ln(j_{0(\text{Facet})}/j_{0(\text{Facet})}^{\text{ref}})$ with crystal facets in Fig. 3b is consistent with the calculated ($E_a^{\text{ref}} - E_a$) (Fig. 3c), indicating that the adiabatic electron-coupled ion transfer model for ion intercalation reaction could be used to accurately describe the kinetics of crystal facets. In the model, different crystal facets are characterized by different WFs and electron interactions with Li^+ . Supplementary Fig. 15 presents the calculated E_a based on the actual WF of the six crystal facets when w_{Li^+} and Δ_0 are set as 0.1 eV and 0.2 eV, respectively. Supplementary Fig. 16 presents the calculated E_a based on actual Δ_0 of the six crystal facets when w_{Li^+} and WF are set as 0.1 eV and 3 eV, respectively. To clearly display the relationship between experimental values and calculated values, the data were replotted in Fig. 3d, where the measured $\ln(j_{0(\text{Facet})}/j_{0(\text{Facet})}^{\text{ref}})$ and calculated ($E_a^{\text{ref}} - E_a$) are set as horizontal and vertical axes, respectively. There is a linear relationship between the calculated ($E_a^{\text{ref}} - E_a$) and measured $\ln(j_{0(\text{Facet})}/j_{0(\text{Facet})}^{\text{ref}})$, which indicates that the WF is an important factor in determining $j_{0(\text{Facet})}$. Note that WF affects the intensity of electric field near the solid-liquid interface, and thus it also impacts the potential distribution in the EDL. A larger WF results in a weaker electric field, larger λ , and larger E_a . A similar linear relationship between measured $\ln(j_{0(\text{Facet})}/j_{0(\text{Facet})}^{\text{ref}})$ and calculated ($E_a^{\text{ref}} - E_a$) based on Δ_0 is also observed, as shown in Fig. 3e, which suggests that both WF and Δ_0 determine the $j_{0(\text{Facet})}$. According to the model, stronger electron interactions lead to smaller E_a . Thus, the slope of the fitting line in Fig. 3d is 0.083, which is larger than 0.039 in Fig. 3e. Comparison of these two slopes implies that WF is the dominant factor in determining the intercalation rates of Li ions for different crystal facets on the NMC811 particles. Note that both values of slope in Fig. 3d and Fig. 3e are in the same order of magnitude with $1/k_B \cdot T$ (0.025), which indicates that the obtained values of WF and Δ_0 are reasonable.

Application of $j_{0(\text{Facet})}$ toward nanostructural design of a high-rate NMC811 electrode

Based on the understanding of the electrochemical kinetics on different facets, we have proposed a nanostructural design for NMC811

materials, which enables both high-capacity and high-rate capabilities simultaneously. Figure 4a shows the schemes of two typical NMC811 electrodes assembled with two types of NMC811 particles, i.e., isotropic NMC811 agglomerate with arbitrary distribution of crystal facets and anisotropic core-shell NMC811 with anisotropic arrangement of the outer shell. The (003) facet of NMC811 positive electrode is perpendicular to the c-axis, which represents the direction of interlayer stacking. Under the synthesis conditions of isotropic NMC811 agglomerate, due to weak interlayer forces, the (003) facet tends to be parallel to the exposed surface of particle during the growth of crystal and forms a large basal plane. Thus, the isotropic NMC811 agglomerate is known as the common commercialized agglomerated particles that were used for high-capacity NMC811 positive electrode, and the latter anisotropic core-shell particles are the high-rate NMC811 materials with remained high-capacity ability because the solid-liquid interface created by the kinetically slowest (003) facet is mostly avoided.

Figure 4b and c exhibit the SEM images of these two kinds of uniform NMC811 particles. Figure 4d shows the HRTEM image, SEM image, and corresponding schematic diagrams of an isotropic NMC811 agglomerate after focused ion beam (FIB) slicing. To manipulate the rate capability, the size of agglomerate particles plays a significant role in Li^+ transportation in the porous electrode and Li^+ diffusion in the solid active particles, and meanwhile the charge transfer kinetics on the particle surface of exposed crystal facets is also critical. As shown in Supplementary Fig. 17, the sizes of the agglomerate particles of the two samples are similar, and thus the effects of the former would be similar. As a result, the effects of latter, i.e., the charge transfer kinetics on the particle surface, would be more sensitive. According to the results of BIB and energy dispersive spectrometer (EDS) analysis (Supplementary Fig. 18 and Supplementary Fig. 19), the Ni, Co, and Mn elements are found to be uniformly distributed within the two types of positive electrodes. The corresponding electrochemo-mechanical simulation indicates the stress distribution of the pristine and fully charged particles (Supplementary Fig. 20 and Supplementary Fig. 21). In the isotropic NMC811 agglomerate, the stress was found to be uniformly distributed in the particles upon fully charged (Supplementary Fig. 20). In the anisotropic core-shell nanostructure, on the other hand, its primary particles are slightly smaller than that in the isotropic agglomerate (Supplementary Fig. 20). More importantly, the electrochemo-mechanical simulation results suggest that the stress of anisotropic core-shell nanostructures is likely to be distributed in the particle center after being fully charged. Such simulated results imply that the anisotropic core-shell nanostructure would be more stable upon cycling owing to less strain variation in the shell regions.

Accordingly, Fig. 4f and Supplementary Fig. 22 present the comparison of cycling performance (low-charge (0.5 C)/fast-discharge (10 C)) for anisotropic core-shell NMC811 and isotropic NMC811 agglomerate (the average result of 5 samples). After 500 cycles at such a high rate, the anisotropic core-shell NMC811 is more stable than the isotropic NMC811, with a capacity retention ratio of greater than 80%. Supplementary Fig. 23 shows the rate performance of the electrodes assembled with two kinds of NMC811 particles (isotropic agglomerates and anisotropic core-shell nanostructures). Figure 4g shows the batteries with intermediate values among the five samples, and the corresponding voltage profiles are shown in Supplementary Fig. 24. The capacity of electrodes assembled with anisotropic core-shell nanostructures is higher than that of electrodes with isotropic agglomerates. The anisotropic core-shell nanostructure exhibits a capacity of 144 $\text{mAh}\cdot\text{g}^{-1}$ at 10 C during the first cycle, while the isotropic sample exhibits only a capacity of 67 $\text{mAh}\cdot\text{g}^{-1}$ at the same rate. As is expected, both NMC811 electrodes exhibit similar capacities at 0.1 C because they are essentially the same NMC811 material with high-capacity storage and delivery. As the discharge rate increases, the electrochemical kinetics determines the capacity of the electrode. Because the diffusion

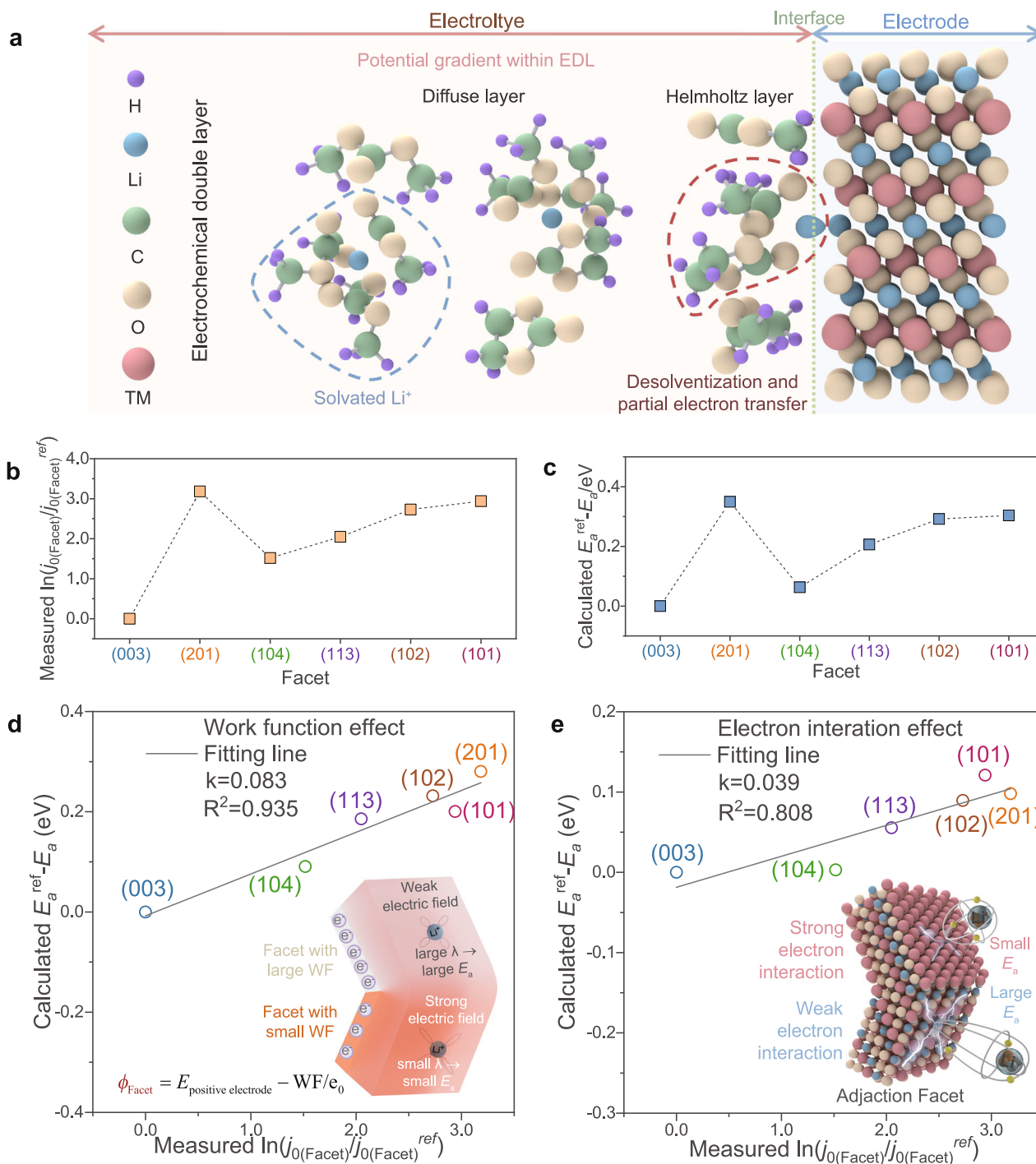


Fig. 3 | Determination of factors that dominate the kinetics of the crystal facets. **a** Schematic diagram of electrochemical double layer model at NMC811-electrolyte interfaces. **b, c** The measured $\ln(j_{0(\text{Facet})}/j_{0(\text{Facet})}^{\text{ref}})$ and calculated ($E_a^{\text{ref}} - E_a$) for the six facets. **d** Linear relationship between the measured $\ln(j_{0(\text{Facet})}/j_{0(\text{Facet})}^{\text{ref}})$ and

the calculated ($E_a^{\text{ref}} - E_a$) with considering the effect of WF, and the schematic diagram of the effect of WF on E_a . **e** Linear relationship between the measured $\ln(j_{0(\text{Facet})}/j_{0(\text{Facet})}^{\text{ref}})$ and the calculated ($E_a^{\text{ref}} - E_a$) with considering the effect of electron interactions, and the schematic diagram of the effect of electron interactions on E_a .

pathways for Li⁺ ions are prone to parallel to the (003) facet (with lower energy barriers for Li⁺ diffusion), the anisotropic core-shell structured NCM811 particles exhibit increased Li⁺ diffusion rate in addition to improved reaction kinetics at the solid-liquid interface. Both of these two factors could contribute to promoted rate capacity in the anisotropic core-shell structured NCM811. As a result, the polarization of electrode with small interfacial impedance is still at a low level, and thus the anisotropic core-shell electrode reaches the cutoff voltage later than the isotropic sample. Therefore, Fig. 4h also shows the comparison of

charge and discharge voltage curves of the two electrodes at 10 C. The state-of-the-art for the high-rate NCM811 electrodes from the literature is listed in Fig. 4i and Supplementary Table 4 (coin-type cells compared)^{24–31}. It suggests that the as-designed NCM811 electrode of anisotropic core-shell nanostructures here highlights specific advantages in capacity at high rates because of the minimized presence of solid-liquid interface created by the kinetically slowest (003) facet. These results also promise a platform to achieve advanced lithium-ion batteries (LIBs) with both high-power and high-energy densities.

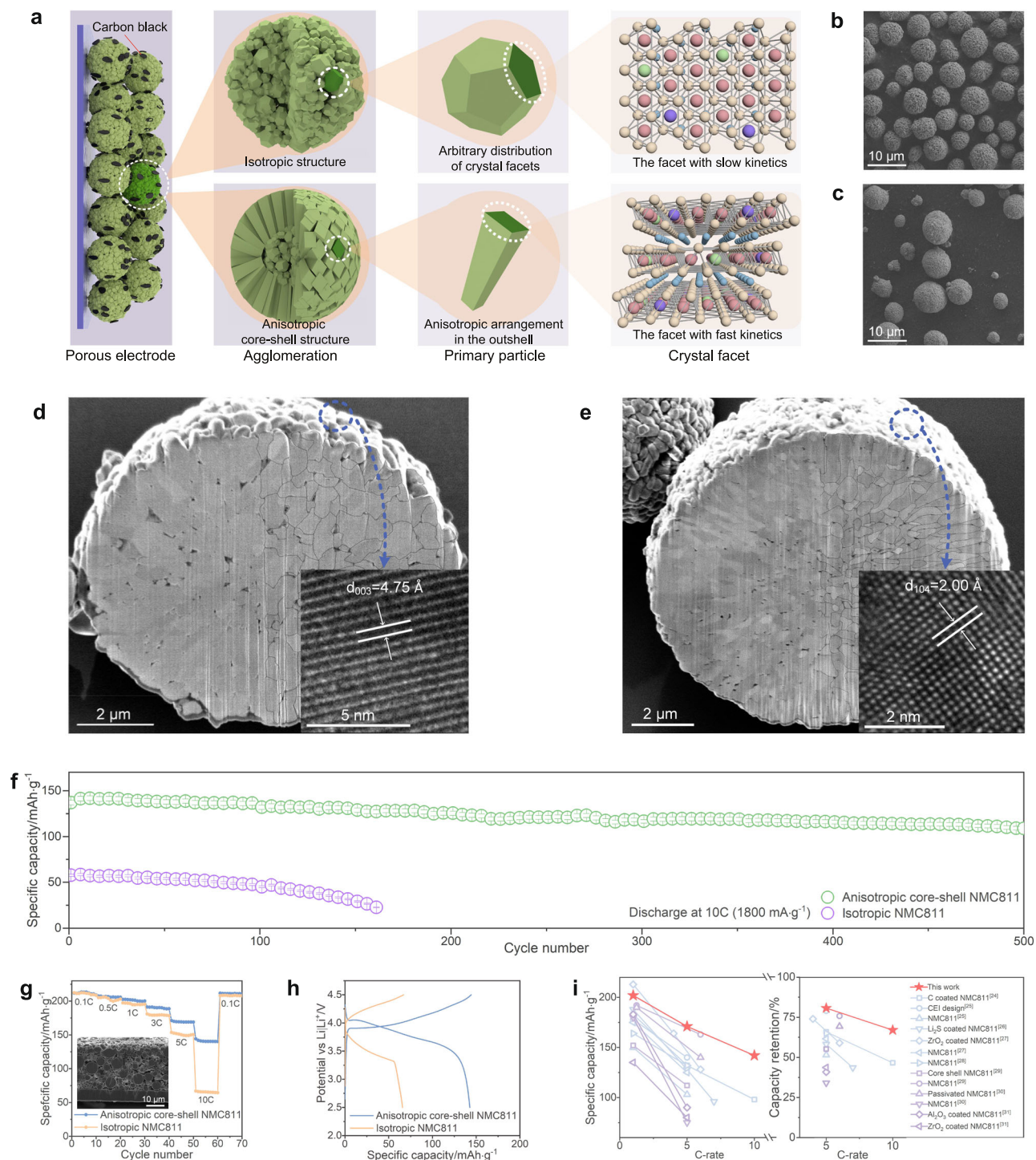


Fig. 4 | Application of $j_{0(\text{Facet})}$ toward designing high-rate NMC811 positive electrode via minimizing the presence of solid-liquid interface created by the kinetically slowest (003) facet. a Schematic diagrams of two kinds of electrodes using agglomerates with isotropic structure and anisotropic core-shell structure. **b, c** SEM images of NMC811 particles with isotropic structure and anisotropic core-shell structure. **d, e** SEM and HRTEM images of isotropic NMC811 agglomerates and anisotropic core-shell NMC811 agglomerates. **f** Long-term cycle performance of anisotropic core-shell NMC811 electrode and isotropic NMC811 electrode (slow

charge at 0.5C/fast discharge at 10C and 1C = 180 $\text{mA}\cdot\text{g}^{-1}$). **g** Rate performance of the cell assembled by NMC811 agglomerates with isotropic structure and anisotropic core-shell structure. **h** The charging and discharging curves of the cell assembled by NMC811 agglomerates with isotropic structure and anisotropic core-shell structure at 10C. **i** Comparison with the rate-performance and capacity retention of other interface-modified NMC811 reported in the literature (the source of the literature data shown in this figure can be found in Supplementary Table 4).

In summary, a quantitative single-particle method was developed to identify the intrinsic electrochemical kinetic parameter j_0 of different crystal facets of NMC811 particles. The $j_{0(201)}$ shows the largest value of $1.50 \text{ mA}\cdot\text{cm}^{-2}$, which is 25-fold larger than $j_{0(003)}$. According to an adiabatic electron-coupled ion transfer model, the difference in the

WF and electron interactions between crystal facet and Li^+ lead to the difference in the kinetics of the crystal facets. Based on such understanding, we have designed an anisotropic core-shell nanostructure for NMC811 positive electrode material to avoid the solid-liquid interface created by kinetically slowest (003) facet. This positive electrode

material exhibits a capacity of 144 mAh·g⁻¹ at 10 C, which is more stable and higher than that of the isotropic NMC811 positive electrode material. This work provides a way to investigate the kinetics of crystal facets and design positive electrode materials with both high-capacity and high-rate capabilities.

Methods

Preparation of Positive Electrode Material

The single crystal LiNi_{0.8}Co_{0.1}Mn_{0.1}O₂ (NMC811) is obtained by high-temperature sintering of Ni_{0.8}Mn_{0.1}Co_{0.1}(OH)₂ precursors. At first, NiSO₄·6H₂O (Aladdin, ≥99.9%), CoSO₄·7H₂O (Aladdin, ≥99.9%) and MnSO₄·5H₂O (Macklin, ≥99.9%) were added into deionized water according to the desired atomic ratio to form an aqueous solution containing 2 mol/L of metal ions. 5 mol/L NaOH solution used as the precipitation agent and 3 mol/L ammonia used as a chelating agent were separately added to the previous mixed salt solution with continuous stirring under an N₂ atmosphere. The environment temperature of coprecipitation operation was controlled at 40 °C and the pH was 10.5. After the washing, filtering, and drying steps, the hydroxide precursor was mixed with LiOH·H₂O (Aladdin, ≥99.9%) according to the mole ratio of Li: M was 1.05:1. The mixture was preliminarily annealed at 500 °C for 5 h, and subsequently calcined at 750 °C for 48 h in an O₂ atmosphere. Finally, the single-crystalline NMC811 particles were obtained. The agglomerates NMC811 positive electrode with isotropic structure was obtained by using Ni_{0.8}Mn_{0.1}Co_{0.1}(OH)₂ precursor which was synthesized under fast stirring in pH of 12 at 50 °C. After being mixed with LiOH·H₂O, the precursor was calcined at 730 °C for 10 h under O₂ flow. To prepare the agglomerates NMC811 positive electrode with anisotropic core-shell structure, the spherical Ni_{0.8}Mn_{0.1}Co_{0.1}(OH)₂ precursor was synthesized in two steps. Firstly, a small amount of precipitant is added to allow the precursor to nucleate under fast stirring in the pH of 12 at 50 °C. Secondly, add precipitants gradually to allow precursors to grow under slow stirring in a pH of 10.5 at 50 °C. Afterward, the reaction was allowed to continue for 48 h. Finally, the anisotropic core-shell structure NMC811 positive electrode was synthesized through the high-temperature solid-phase reaction. To investigate the effect of pH changes on the distribution of transition metal elements, the two types of agglomerates were cut using the broad ion beam (BIB). The corresponding cross-sectional SEM images and the EDS of two samples indicate that the Ni, Co, and Mn elements are uniformly distributed within the two types of positive electrodes (Supplementary Fig. 18 and Supplementary Fig. 19).

Fabrication of the coin cell

The coin half-cells (LIR2032 with stainless steel spring) were assembled by using the NMC811-based positive electrode, lithium metal (Aladdin, ≥99.9%) negative electrode, and Celgard 2325 separator with the thickness of ~20 μm. The lithium metal negative electrode with the thickness of 1 mm and diameter of 14 mm was scraped using a knife to remove the oxide layer before use. 1 M LiPF₆ in ethylene carbonate (EC) / ethyl methyl carbonate (EMC) (1:1, by wt) was used as the electrolyte (purchase from Aladdin). The electrolyte was stored in a glove box filled with dry Ar gas and kept at a temperature of 20 °C ± 1 °C. The NMC-based positive electrode consists of 85 wt% active material, 5 wt% polyvinylidene fluoride (PVdF) (Macklin, ≥99.9%), and 10 wt% carbon black (Aladdin, ≥99.9%). The thickness of aluminum current collector (Wuxing Aluminum Co., Ltd., ≥99%) is 12 μm. Firstly, the powder mixture was dispersed in *n*-methyl pyrrolidone solvent (NMP) (Aladdin, ≥99%) and mixed in an agate mortar in air at 20 °C ± 1 °C. Then the obtained slurry was coated on the aluminum foil by doctor blading at a 60 μm wet thickness. The coated sheets were dried under the dynamic vacuum at 80 °C for 10 h, after which it was punched into 12 mm diameter electrodes using coin cell electrode punching machine. And then cylindrically rolled at 150 MPa, and finally further dried under the dynamic vacuum at 80 °C for 12 h. The fabrication of coin cells was carried out in a glove box filled with Ar gas (the concentrations of water and oxygen are

below 0.1 ppm). During the assembly of coin cells, sufficient electrolyte should be added to ensure that the electrodes are completely saturated.

Measurement of the coin batteries

The assembled coin batteries (~30 μm and 6.3 mg·cm⁻²) were settled for 5 h and then were tested using a battery charged/discharged equipment (CT-4000, Neware Technology Limited). The battery charged/discharged equipment is located in a room with air conditioning running and the environment temperature is maintained at 20 °C ± 1 °C. The testing steps are as follow. The coin batteries were pre-cycled for an initial two cycles at 0.1 C rate between 2.5 and 4.5 V (1 C = 180 mA·g⁻¹). For the long-term cyclic test, the cells (electrode thickness ~10 μm and 2.1 mg·cm⁻²) were subjected to the same pre-cycle, then was cycled for 500 cycles (with a protocol of 0.5 C charging to 4.5 V and 10 C discharge to 2.5 V). The specific capacity is obtained by dividing the total capacity of coin cell by the mass of positive electrode material.

Measurement of exchange charge density of different facets

$j_{O(\text{Facet})}$

Firstly, X-ray diffraction (XRD) analysis was carried out on NMC811 powder. The cell parameters of the material were obtained from the refined XRD pattern. The standard angles between various crystal facets can be obtained from the reconstructed NMC811 crystal structures. Secondly, several images of a defined particle were taken from various viewpoints in a scanning electron microscope (SEM) equipped with a focused ion beam (FIB). It aims to record the geometrical features of the particle, and these SEM images can be used later to assist in the identification of the facets. Afterward, a small portion at the edge of the particle was excised for high-resolution transmission electron microscope (HRTEM) characterization to identify one to two crystal facets. It is important to record the face of the particle corresponding to the crystal facet characterized by the HRTEM. In the HRTEM operation, crystalline axis alignment was performed according to the routine HRTEM tuning method. Then, the specific lattice stripes that were parallel to the particle edge profile were selected. Note that additional particles should be employed if the specific lattice stripes with the aforementioned feature could not be acquired (Caution: more particles might be repeated in the HRTEM experiments to achieve the goal). In the following operation, the TEM sample was rotated along the axis in the direction of the lattice stripe until the exposed facet was almost perpendicular to the observed angle, and thus the rotation angle was recorded. The exposed crystal facets were identified by matching the rotation angles acquired from HRTEM with the standard angles from XRD. The accuracy of measured angles using such a rotatable sample holder depends on the shape of the samples (e.g., flatness of exposed facets) and the proficiency of the tester (Caution: more attempts might be required in the HRTEM experiments to achieve the goal, and the errors in the obtained angles would influence the identifying accuracy of the facets). In the case that the angles between a given crystal facet and multiple crystal facets is very close, more possible facets may be identified and such uncertainty could be addressed via introducing three-dimensional (3D) construction of the particle. Compared to the established approaches in the previous studies^{32–34}, the method in the present study is a feasible way to capture the information from an arbitrary facet that is not perpendicular to the zone axis. Thirdly, the particle was welded to a resin-coated tungsten probe to prepare a single-particle electrode using the SEM equipped with FIB⁶. The process that is accomplished by using a deposition and FIB etching procedure during the single particle electrode preparation process, the coating layer on the tip of the tungsten needle was first removed by ion beam, and then, the NMC811 particle was welded with the needle by sputtering Pt. It is worth noting that under the premise of ensuring the welding strength, the area of the exposed tungsten

needle and the deposited Pt must be as small as possible to avoid interference with the electrochemical measurement. The single-particle electrode was subjected to electrochemical impedance spectroscopy (EIS) measurement using a three-electrode system. Firstly, all the pristine NMC811 particles were scanned at 0.05 mV·s⁻¹ via one cycle in the electrode potential range OCV~4.0 V (vs. Li|Li⁺) prior to electrochemical impedance measurements, with purpose of cleaning the particle surface. Then, the particles were delithiated to 3.5 V with a current of 0.1 nA. At this potential, the pristine arrangement of atoms could be largely reserved, and meanwhile the blocking behavior could be partially eliminated since the voltage platform of NCM811 positive electrode is higher than 3.6 V. The charge transfer resistance of the particle ($(R_{CT})_{\text{Particle}}$) was extracted from the EIS by fitting an equivalent circuit and the exchange current of the particle ($i_{0(\text{Particle})}$) was obtained using the following equation:

$$i_{0(\text{Particle})} = \frac{RT}{nF(R_{CT})_{\text{Particle}}} \quad (5)$$

where R is the gas constant, T is the temperature, n is the number of electrons transferred in the reaction, and F is the Faraday constant. Due to the small charging voltage, there is almost no pronounced CEI formed on the surface of positive-electrode particles, and thus the resistance of CEI is not considered³⁵. As a type of ultra-microelectrode, the single-particle electrode generates an extremely small current, and therefore the IR drop of the electrode and the concentration polarization of electrolyte to be neglected. In addition, only a small stimulation signal of 5 mV is applied during the EIS measurement, which further reduces the current that travels through the entire single-particle electrode. Therefore, the position of W-tip, i.e., changes in the resistance of different facets, will not significantly affect the measurement results. The entire electrode system was shielded from vibration and electromagnetic interference. Fourthly, the single-particle electrode is cleaned by immersion in acetonitrile after testing to remove residual electrolytes. The single-particle electrode is then transferred to an SEM equipped with FIB for 3D reconstruction. The area of each facet and the angle between every two facets were recorded by measuring the 3D reconstructed image of the particle. These angles were further matched with the standard angles from XRD to identify the types of exposed facets (Caution: more attempts should be repeated if any exposed facet is not well matched during this calibration process). Finally, the areas and types of each facet of the individual particle were obtained. It is assumed that the different crystal facets of a particle do not interact with each other when the reaction occurs. The relationship between these facets is equivalent to the parallel relationship in a circuit. Therefore, the exchange current density for each facet ($j_{0(\text{Facet})}$) can be obtained using the following equation:

$$\frac{nF}{RT} \sum_{i=1}^n S_{(\text{Facet})}^i j_{0(\text{Facet})}^i = \frac{nF}{RT} i_{0(\text{Particle})} = \frac{1}{(R_{CT})_{\text{Particle}}} \quad (6)$$

where $S_{(\text{Facet})}$ is the area of facet and i represents different facets. It is essentially an inverse step when calculating the $(R_{CT})_{\text{Particle}}$ using the $j_{0(\text{Facet})}$. Firstly, the type and area of each crystal facet of a defined particle were identified using single particle measurements. Afterward, the $i_{0(\text{Particle})}$ was calculated using the Eq. (6). Finally, the $(R_{CT})_{\text{particle}}$ was calculated by Eq. (5).

There are defects in the crystal structure as well as uneven areas on the surface of the NMC811 positive electrode. This feature is common in commercial crystalline materials³⁶. The defects and uneven areas may lead to some deviations between the measured $j_{0(\text{Facet})}$ and the real $j_{0(\text{Facet})}$. Note that the use of single-particle measurements to investigate the kinetics of crystal facets remarkably reduces the

difficulty of the preparation of samples, and this method is highly feasible and robust.

Electrochemo-mechanical model

The stress distributions of NMC811 particles with two types of structures under different Li⁺ concentrations were simulated by Comsol Multiphysics 5.6. A simplified chemo-mechanical model was employed to simulate the electrochemo-mechanical stress distribution in different particle structures. In such electrochemo-mechanical model, the agglomerate particles assembled with primary particles were assumed to be homogeneous, and these agglomerate particles were assumed to present a uniform feature, with different characteristics according to the anisotropic crystal orientation. Meanwhile, the effect of volume expansion induced by lithium-ion intercalation on the mechanical stress distribution was considered. However, the impact of mechanical deformation on the diffusion process is not considered. In the bulk particle, the electrochemo-mechanical coupled equations could be used to determine the stress distribution and anisotropic expansion, as shown in Eqs. (7) and (8).

$$\sigma_x = \frac{E}{1-\nu^2} (\epsilon_x + \nu\epsilon_y) - \frac{E\alpha c_{Li}}{1-\nu} \quad (7)$$

$$\sigma_y = \frac{E}{1-\nu^2} (\epsilon_y + \nu\epsilon_x) \quad (8)$$

where expansivity α is partial molar volume of Li atom, which can be also used to describe the expansivity of grains in the particles. E and ν are Young's modulus and Poisson ratio of grains in the particles, respectively. The parameters values of the electrochemo-mechanical model are $\alpha = 1.23 \times 10^{-5} \text{ m}^3 \cdot \text{mol}^{-1}$, $E = 140 \text{ GPa}$, $\nu = 0.2166$ ³⁷. In the small part of boundary of secondary particle, the fixed support was applied and free boundary is applied on the others. The coordinate transformation was used to simulate the different orientation of the primary particles, as shown in Eq. (9).

$$\begin{bmatrix} \epsilon_{x'} \\ \epsilon_{y'} \end{bmatrix} = \begin{bmatrix} \epsilon_x & \epsilon_y \end{bmatrix} \begin{bmatrix} \cos \theta \\ \sin \theta \end{bmatrix} \quad (9)$$

where θ is used to describe the angle of the primary particle. In the anisotropic core-shell structure NCM811 particle, the θ of primary particles in the shell were selected in order as shown in Supplementary Fig. 21, and the θ of primary particles in the core were selected randomly. In the isotropic structure NCM811 particle, on the other hand, the θ of all the primary particles were selected randomly. Finally, the effect of stress on the ion diffusion has been evaluated using Eq. (10):

$$\epsilon = \frac{\sigma}{E} \quad (10)$$

The results showed that the largest deformation of NMC811 lattice caused by the stress in the particle was <0.03%. Therefore, the effect of stress on ion diffusion could be ignored in this case.

Calculation of E_a

The expression of E_a is based on the microscopic Hamiltonian model established by Huang³⁸ for dealing with hydrogen reactions in alkaline media. In contrast to the hydrogen reactions, the molecules that make up the solvation shell have no charges for the intercalation reaction. The work that is required to move solvent molecules in the electric field is zero. The commonly used lithium salt (LiPF₆) in LIBs is supposed to be completely ionized in the electrolyte. Therefore, the

equation of E_a can be simplified as:

$$E_a = \frac{(\lambda + e_0\eta + w_{Li^+})^2}{4\lambda} + E_e(\Delta_0), \quad (11)$$

where λ is solvent reorganization energy, e_0 is the elementary charge, η is the overpotential. Typically, w_{Li^+} is the electrostatic work consumed in moving Li^+ from the bulk solution to the transition state, which can be obtained from an established EDL model³⁹. $E_e(\Delta_0)$ is the part of electronic interaction and is described as:

$$E_e(\Delta_0) \approx -\frac{\Delta_0}{2\pi} \ln \left(1 + \left(\frac{\epsilon_a^{\text{eff}}}{\Delta_0} \right)^2 \right), \quad (12)$$

$$\epsilon_a^{\text{eff}} \approx \epsilon_a, \quad (13)$$

where ϵ_a is the energy of $Li\ 2s$ orbital and Δ_0 is the integral strength of electronic interaction, which can be calculated using a DFT-parameterized model as³⁸:

$$\rho_{2s} = \frac{1}{\pi} \frac{\Delta}{[\epsilon - (\epsilon' + \Lambda)]^2 + \Delta^2}, \quad (14)$$

where Δ and Λ are the chemisorption functions, ρ_{2s} is the DOS of $2s$ orbital of Li near the surface of a target facet, and $\epsilon' = \epsilon_a - 2\lambda q - e_0\phi$ in which ϵ_a denotes the energy of the $2s$ orbital of the Li atom, q is the number of charges, and ϕ is the electric potential.

$$\Delta = \sum_k |V_k|^2 \pi \rho_k(\epsilon), \quad (15)$$

where k means the s , p , and d bands of facet, $|V_k|^2$ is the strength of electronic interactions exerted by different bands, and ρ_k is the DOS of different bands.

$$\Lambda = \frac{1}{\pi} \mathcal{P} \int \frac{\Delta}{\epsilon - \epsilon'} d\epsilon' \quad (16)$$

where \mathcal{P} is the Cauchy principal part. Note that ρ_k adopts the value at the Fermi level and $|V_k|^2$ adopts the value at 1 nm for different bands when calculating Δ_0 using Eq. (15).

Calculation of λ

The λ adopts the form in the derived hybrid quantum-classical model²⁰:

$$\lambda = \frac{(\mathbf{H}^{\text{in}})_{22} - (\mathbf{H}^{\text{in}})_{21} - (\mathbf{H}^{\text{in}})_{12} + (\mathbf{H}^{\text{in}})_{11}}{2}, \quad (17)$$

The \mathbf{H}^{in} represents the Hamilton operator of inertial (slow) part corresponding to the nuclear polarization of the two-stage Debye charging approach. The subscript numbers imply the elements of the square matrix in the second order. Meanwhile, the 1 and 2 show the physical implication of initial and terminal states during the charge transfer process. The \mathbf{H}^{in} can be calculated using the following equation:

$$(\mathbf{H}^{\text{in}})_{ij} = (\mathbf{H})_{ij} - (\mathbf{H}^\infty)_{ij}, \quad (18)$$

The \mathbf{H}^∞ represents the Hamilton operator of non-inertial (fast) part corresponding to the electronic polarization of the two-stage Debye charging approach. The $(\mathbf{H})_{ij}$ and $(\mathbf{H}^\infty)_{ij}$ can be obtained from the EDL model. The EDL is controlled by the simplified volumetric Gibbs free-energy density functional. In this model, the volume effect of the species within EDL is considered.

Calculation of $(\mathbf{H})^{\text{in}}$

The $(\mathbf{H})_{ij}$ and $(\mathbf{H}^\infty)_{ij}$ can be expressed as:

$$(\mathbf{H})_{ij} = - \int \phi_{ij} \sigma_{i,ij} dS_I - \int \phi_{ij} \sigma_{F,ij} dS_F, \quad (19)$$

$$(\mathbf{H}^\infty)_{ij} = - \int \phi_{ij}^\infty \sigma_{i,ij} dS_I - \int \phi_{ij}^\infty \sigma_{F,ij} dS_F \quad (20)$$

where ϕ is the electrical potential, σ is the surface charge density, and S is the area. The subscript I and F represents Li^+ and crystal facets respectively. Note that σ_F is determined by the electrical potential of crystal facets which is kept constant during the reaction. Therefore the last term in Eqs. (19) and (20) is zero.

The $(\mathbf{H})_{ij}$ and $(\mathbf{H}^\infty)_{ij}$ can be obtained from an EDL model established by Huang et al.⁴⁰. In this model, the volume effect of the particles is considered. The EDL is controlled by the simplified volumetric Gibbs free-energy density functional

$$f = e_0\phi(N_c - N_a) - \frac{\epsilon_\infty E^2}{2} - \frac{1}{\beta} N_s \ln \left(\frac{\sinh(pE\beta)}{pE\beta} \right) + \frac{1}{\beta} \ln \frac{N!}{N_a! N_c! N_s!}, \quad (21)$$

where e_0 is the elemental charge, N is the number of particles, ϵ_∞ is the non-inertial optical component of dielectric constant, E is the electric field, p is the dipole moment of the electrolyte solvent, and β is the inverse thermal energy. The subscripts c , a , and s of N represent cations, anions, and solvent molecules. The N_c and N_a are determined by the electrochemical potential in the EDL which is equal to the electrochemical potential in the bulk of electrolyte

$$\frac{\partial f}{\partial N_c} = \left(\frac{\partial f}{\partial N_c} \right)_{\text{bulk}} \quad (22)$$

$$\frac{\partial f}{\partial N_a} = \left(\frac{\partial f}{\partial N_a} \right)_{\text{bulk}} \quad (23)$$

Meanwhile, $N = N_c + N_a + N_s$.

The free-energy density function is submitted to variational analysis, which leads to the Euler-Lagrange equation in terms of ϕ :

$$\frac{\partial f}{\partial \phi} - \frac{\partial}{\partial x} \left(\frac{\partial f}{\partial E} \right) = 0. \quad (24)$$

Thus, the double layer on the electrolyte side is governed by the modified Poisson-Boltzmann equation in which the volume effect of the particle is taken into account. In the bulk of electrolytes, the ϕ is set as 0, which is defined as a reference potential. On the surface of particles, the potential (ϕ_{app}) of the facet is determined by the work function (WF) of crystal facet and the potential of NMC811 positive electrode ($E_{\text{Positive-electrode}}$) as Eq. (23):

$$\phi_{\text{Facet}} = E_{\text{Cathode}} - \text{WF}/e_0 \quad (25)$$

The $E_{\text{Positive-electrode}}$ is set as 5.3 V (vs. vacuum).

Material characterizations

The microstructure of the samples was characterized by field emission SEM (Helios Nanolab G3 UC) and TEM (Jem-2100F Jeol). The microstructure of crystal facets was characterized using a cryogenic scanning transmission electron microscope (cryo-STEM) (JEM-1400Flash (HC) 120KV). The phase composition of the samples was characterized by XRD (BRUKER D8 Series). The agglomerate size of NMC811 positive electrode with isotropic structure and anisotropic core-shell structure was analyzed using a laser particle size analyzer.

The EDS sample preparation

The two types of NMC811 positive-electrode materials with isotropic structure and anisotropic core-shell structure were prepared as thin porous electrodes. After cutting using BIB, the porous electrodes were transferred to a SEM for EDS analysis.

Cryo-STEM sample preparation

The NMC811 single particle was cleaned with acetonitrile after being tested and then transferred into a FIB-capable SEM using an Ar gas-filled vessel. After cryo-sectioning in FIB, the slice was transferred to cryo-STEM for characterization. The samples were only briefly exposed to air during installation in the SEM and Cryo-STEM.

Design and fabrication of the three-electrode single-particle cell

The three-electrode system adopts a single-particle electrode as a working electrode, lithium metal as a counter electrode and the reference electrode⁶. The working electrode consists of a resin-coated tungsten needle welded with a single crystal NMC811 particle, a process that is accomplished by using a deposition and FIB etching procedure during the single particle electrode preparation process. The coating layer on the tip of the tungsten needle was first removed by ion beam, and then, the NMC811 particle was welded with the needle by sputtering Pt. Note that the area of the exposed tungsten needle and the deposited Pt must be as small as possible to avoid interference with the electrochemical measurement under the promise of ensuring the welding strength. 1 M LiPF₆ in ethylene carbonate (EC) / ethyl methyl carbonate (EMC) (1:1, by wt) was used as the electrolyte (purchase from Aladdin).

Electrochemical measurements

The measurement of EIS spectra and charge in the three-electrode single-particle battery was carried out on the electrochemical workstation (VersaSTAT 3F) equipped with VersaSTAT LC. The EIS measurement was performed in the frequency range from 10⁵ Hz to 10⁻¹ Hz (7 points per decade). A voltage of 10 mV was selected as the perturbation signal for EIS measurements. Prior to the single-particle EIS measurement, the NCM811 particle surface were pre-cleaned with one cycle of cyclic voltammetry (CV) at a scan rate of 0.05 mV·s⁻¹ in the electrode potential range OCV-4.0 V (vs. Li|Li⁺). Then, the particles were charged to 3.5 V with a current of 0.1 nA. After completing the CV treatment, the open-circuit potential of single-particle electrode was measured. When the change in open-circuit potential is less than 10 mV within 30 min, the EIS measurement was performed. Therefore, the EIS measurement is conducted under quasi-stationary potential conditions. All the single-particle electrochemical measurements were performed in a glove box with an Ar atmosphere (the concentrations of water and oxygen are below 0.1 ppm), and the devices were placed in a vibration-free and electromagnetic-shielded environment. The glove box is located in a room with air conditioning running and the environment temperature is maintained at 20 °C ± 1 °C.

The DFT calculation

All computational simulations conducted in this work are based on the density functional theory (DFT) framework, with specific calculations implemented through the Vienna Ab initio Simulation Package (VASP). For the description of the exchange-correlation potential, the generalized gradient approximation proposed by Perdew, Burke, and Ernzerhof-referred to as GGA-PBE-is adopted. To handle the interactions existing between ion cores and valence electrons, the projector augmented-wave (PAW) method is utilized throughout the entire calculation process. A fixed plane-wave cutoff energy of 500 eV is set to ensure the accuracy of the electronic structure calculations. For the structural relaxation of the given models, the relaxation process is continued until two key convergence criteria are satisfied: first, the Hellmann-Feynman forces

acting on each atom are reduced to a value smaller than -0.02 eV/Å, and second, the variation in the total energy of the system is minimized to less than 10⁻⁵ eV. During the structural relaxation stage, the Brillouin zone is sampled using a Γ -centered k-point grid with a mesh density of 2 × 2 × 1. Additionally, to avoid the occurrence of spurious interlayer interactions caused by the periodic boundary conditions, a vacuum layer with a thickness of ~40 Å is introduced in the direction perpendicular to the material surface.

Data availability

The authors declare that all data are available in the main text or the supplementary materials, and the Source Data is provided with this manuscript. Source data are provided with this paper.

References

1. Liu, Y., Zhu, Y. & Cui, Y. Challenges and opportunities towards fast-charging battery materials. *Nat. Energy* **4**, 540–550 (2019).
2. Tavassol, H., Jones, E. M. C., Sottos, N. R. & Gewirth, A. A. Electrochemical stiffness in lithium-ion batteries. *Nat. Mater.* **15**, 1182–1187 (2016).
3. Yu, J., Wei, Y. & Meng, B. Homogeneous distributed natural pyrite-derived composite induced by modified graphite as high-performance lithium-ion batteries anode. *Int. J. Miner. Metall. Mater.* **30**, 1353–1362 (2023).
4. Li, W., Erickson, E. M. & Manthiram, A. High-nickel layered oxide cathodes for lithium-based automotive batteries. *Nat. Energy* **5**, 26–34 (2020).
5. Lin, R. et al. Hierarchical nickel valence gradient stabilizes high-nickel content layered cathode materials. *Nat. Commun.* **12**, 2350 (2021).
6. Li, X. et al. Correlating electrochemical kinetic parameters of single LiNi_{1/3}Mn_{1/3}Co_{1/3}O₂ particles with the performance of corresponding porous electrodes. *Angew. Chem. Int. Ed.* **61**, e202205394 (2022).
7. Miß, V., Ramanayagam, A. & Roling, B. Which exchange current densities can be achieved in composite cathodes of bulk-type all-solid-state batteries? A comparative case study. *ACS Appl. Mater. Interfaces* **14**, 38246–38254 (2022).
8. Chen, R. et al. Spatiotemporal imaging of charge transfer in photocatalyst particles. *Nature* **610**, 296–301 (2022).
9. Yamamoto, T. et al. Characterization of the depth of discharge-dependent charge transfer resistance of a single LiFePO₄ particle. *Anal. Chem.* **93**, 14448–14453 (2021).
10. Mefford, J. T. et al. Correlative operando microscopy of oxygen evolution electrocatalysts. *Nature* **593**, 67–73 (2021).
11. Sambur, J. B. et al. Sub-particle reaction and photocurrent mapping to optimize catalyst-modified photoanodes. *Nature* **530**, 77–80 (2016).
12. Wen, B. et al. Ultrafast ion transport at a cathode–electrolyte interface and its strong dependence on salt solvation. *Nat. Energy* **5**, 578–586 (2020).
13. Tsai, P.-C. et al. Single-particle measurements of electrochemical kinetics in NMC and NCA cathodes for Li-ion batteries. *Energ. Environ. Sci.* **11**, 860–871 (2018).
14. Jizhou, L. et al. Dynamics of particle network in composite battery cathodes. *Science* **376**, 517–521 (2022).
15. Du, M., Lü, H. & Du, K. Upcycling the spent graphite/LiCoO₂ batteries for high-voltage graphite/LiCoPO₄-co-workable dual-ion batteries. *Int. J. Miner. Metall. Mater.* **31**, 1745–1751 (2024).
16. Wu, M. et al. Seeded growth of large single-crystal copper foils with high-index facets. *Nature* **581**, 406–410 (2020).
17. Ke, J. et al. Facet-dependent electrooxidation of propylene into propylene oxide over Ag₃PO₄ crystals. *Nat. Commun.* **13**, 932 (2022).
18. Wang, S. et al. Identifying the geometric catalytic active sites of crystalline cobalt oxyhydroxides for oxygen evolution reaction. *Nat. Commun.* **13**, 6650 (2022).

19. Selcuk, S. & Selloni, A. Facet-dependent trapping and dynamics of excess electrons at anatase TiO₂ surfaces and aqueous interfaces. *Nat. Mater.* **15**, 1107–1112 (2016).
20. He, J., Yang, L., Huang, J., Song, W.-L. & Chen, H.-S. Hybrid quantum-classical model of mechano-electrochemical effects on graphite-electrolyte interfaces in metal-ion batteries. *Extrem. Mech. Lett.* **59**, 101971 (2023).
21. Wang, X., Huang, J., Liu, Y. & Chen, S. The decisive role of electrostatic interactions in transport mode and phase segregation of lithium ions in LiFePO₄. *Chem. Sci.* **14**, 13042–13049 (2023).
22. Fragedakis, D. et al. Theory of coupled ion-electron transfer kinetics. *Electrochim. Acta* **367**, 137432 (2021).
23. Bazant, M. Z. Unified quantum theory of electrochemical kinetics by coupled ion-electron transfer. *Faraday Discuss.* **246**, 60–124 (2023).
24. Liang, J. et al. Coating Ni-rich cathode with an amorphous carbon for improving the stability and electrochemical performance. *Compos. Commun.* **36**, 101356 (2022).
25. Hou, W. et al. High-voltage nickel-rich layered cathodes in lithium metal batteries enabled by a sulfolane/fluorinated ether/fluoroethylene carbonate-based electrolyte design. *J. Power Sources* **517**, 230683 (2022).
26. Wang, X. et al. High-performance LiNi_{0.8}Mn_{0.1}Co_{0.1}O₂ cathode by nanoscale lithium sulfide coating via atomic layer deposition. *J. Energy Chem.* **69**, 531–540 (2022).
27. Jo, S.-J., Hwang, D.-Y. & Lee, S.-H. Use of Zirconium dual-modification on the LiNi_{0.8}Co_{0.1}Mn_{0.1}O₂ cathode for improved electrochemical performances of Lithium-ion batteries. *ACS Appl. Energ. Mater.* **4**, 3693–3700 (2021).
28. Azhari, L. et al. Underlying limitations behind impedance rise and capacity fade of single crystalline Ni-rich cathodes synthesized via a molten-salt route. *J. Power Sources* **545**, 231963 (2022).
29. Dong, X. et al. Enhanced high-voltage cycling stability of Ni-rich cathode materials via the self-assembly of Mn-rich shells. *J. Mater. Chem. A* **7**, 20262–20273 (2019).
30. mps#12345Liu, W. et al. Functional Passivation Interface of LiNi_{0.8}Co_{0.1}Mn_{0.1}O₂ toward Superior Lithium Storage. *Adv. Funct. Mater.* **31**, 2008301 (2021).
31. Gao, Y., Park, J. & Liang, X. Comprehensive study of Al- and Zr-modified LiNi_{0.8}Mn_{0.1}Co_{0.1}O₂ through synergy of coating and doping. *ACS Appl. Energ. Mater.* **3**, 8978–8987 (2020).
32. Kong, L. et al. Realizing unassisted photo-charging of Zinc-air batteries by anisotropic charge separation in photoelectrodes. *Adv. Mater.* **35**, 2304669 (2023).
33. Qu, J. et al. Determination of crystallographic orientation and exposed facets of titanium oxide nanocrystals. *Adv. Mater.* **34**, 2203320 (2022).
34. Yin, Y. et al. Facet-dependent reactivity of α-Fe₂O₃ nanosheet on reactive oxygen species generation in Fenton-like process. *Appl. Catal. B-Environ.* **340**, 123165 (2024).
35. Xu, K. et al. *Electrolytes, Interfaces And Interphases: Fundamentals And Applications In Batteries*. Ch. 3. (Royal Society of Chemistry Press, UK, 2023).
36. Yan, Y., Jin, Z. & Zhang, H. Recent progresses in thermal treatment of β-Ga₂O₃ single crystals and devices. *Int. J. Miner. Metall. Mater.* **31**, 1659–1677 (2024).
37. Xu, R. et al. Heterogeneous damage in Li-ion batteries: experimental analysis and theoretical modeling. *J. Mech. Phys. Solids* **129**, 160–183 (2019).
38. Huang, J., Li, P. & Chen, S. Quantitative understanding of the sluggish kinetics of hydrogen reactions in alkaline media based on a microscopic Hamiltonian model for the Volmer step. *J. Phys. Chem. C* **123**, 17325–17334 (2019).
39. He, J., Yang, L., Huang, J., Song, W.-L. & Chen, H.-S. Hybrid quantum-classical treatment of lithium ion transfer reactions at graphite-electrolyte interfaces. *J. Power Sources* **564**, 232880 (2023).
40. Huang, J., Li, P. & Chen, S. Potential of zero charge and surface charging relation of metal-solution interphases from a constant-potential jellium-Poisson-Boltzmann model. *Phys. Rev. B* **101**, 125422 (2020).

Acknowledgements

This study was supported by National Natural Science Foundation of China (No. 92475202), the Key-Area Research and Development Program of Guangdong Province (Grant No. 2023B0909050004), the Joint Science Foundation of Gansu Province (24JRRA822), the Science and Technology Project of Gansu province (24RCKA004), and Southern Marine Science and Engineering Guangdong Laboratory (Zhuhai) (SML2023SP243). The authors acknowledge Dr N.L., Dr J.H. and Dr Z.Y.L. for helpful discussions and acknowledge X.D.X. for landscaping the schematic diagrams.

Author contributions

S.Q.J., D.F. and W.L.S. conceived the project, and proposed the experiments. X.L. and L.Y. performed single-particle measurements, modeling, and data analysis. H.J. participated in theoretical modeling of the kinetics of crystal facets. X.L. and W.L.S. proposed the particle nanostructures. X.L. carried out the nanomaterial synthesis and battery experiments. H.S.C. and L.Y. established the models for simulating the stress distribution within the particles. S.Q.J., X.L., W.L.S., D.F. and H.J. analysed the modeling and experimental results. S.Q.J., W.L.S., and H.S.C. acquired the funding. All the authors discussed the results and co-wrote and revised the manuscript.

Competing interests

The authors declare no competing interests.

Additional information

Supplementary information The online version contains supplementary material available at <https://doi.org/10.1038/s41467-025-65068-5>.

Correspondence and requests for materials should be addressed to Hao-Sen Chen, Wei-Li Song or Shuqiang Jiao.

Peer review information *Nature Communications* thanks Dong Su and the other anonymous reviewer(s) for their contribution to the peer review of this work. A peer review file is available.

Reprints and permissions information is available at <http://www.nature.com/reprints>

Publisher's note Springer Nature remains neutral with regard to jurisdictional claims in published maps and institutional affiliations.

Open Access This article is licensed under a Creative Commons Attribution-NonCommercial-NoDerivatives 4.0 International License, which permits any non-commercial use, sharing, distribution and reproduction in any medium or format, as long as you give appropriate credit to the original author(s) and the source, provide a link to the Creative Commons licence, and indicate if you modified the licensed material. You do not have permission under this licence to share adapted material derived from this article or parts of it. The images or other third party material in this article are included in the article's Creative Commons licence, unless indicated otherwise in a credit line to the material. If material is not included in the article's Creative Commons licence and your intended use is not permitted by statutory regulation or exceeds the permitted use, you will need to obtain permission directly from the copyright holder. To view a copy of this licence, visit <http://creativecommons.org/licenses/by-nc-nd/4.0/>.

© The Author(s) 2025